Nanofiltration Membranes Based on Rigid Star Amphiphiles

Yunyi Lu,[†,§] Tasuma Suzuki,[‡,§] Wei Zhang,[†] Jeffrey S. Moore,*[,†,§] and Benito J. Mariñas[‡,§]

Departments of Chemistry and Materials Science and Engineering, University of Illinois, 600 South Mathews Avenue, Urbana, Illinois 61801, Department of Civil and Environmental Engineering, University of Illinois, 205 North Mathews Avenue, Urbana, Illinois 61801, and Center of Advanced Materials for the Purification of Water with Systems, University of Illinois at Urbana−Champaign, Urbana, Illinois 61801

Received January 22, 2007

Rigid star amphiphiles (RSAs) of nanoscale dimension were synthesized and used to fabricate a new generation of nanofiltration (NF) membranes. NF membranes were prepared by direct percolation of methanol solutions of the RSAs through an asymmetric polyethersulfone (PES) support film that had been previously conditioned with methanol and cross-linked polyvinyl alcohol (PES-MeOH-PVA support). The resulting RSA membranes (RSAMs) have been shown to exhibit significantly enhanced water permeability while maintaining high rejection of water contaminants compared to commercial NF membranes. The RSAMs were characterized with the goal of elucidating the structural changes brought about by deposition of RSA. Characterization techniques used included attenuated total reflectance Fourier transform infrared (ATR-FTIR) spectrometry, field emission scanning electron microscopy (FE-SEM), atomic force microscopy (AFM), X-ray photoelectron spectroscopy (XPS), confocal microscopy, Rutherford backscattering spectrometry (RBS), and gas adsorption/desorption analyses. Results suggest that the RSAs produce a uniform, ultrathin active layer atop the PES-MeOH-PVA support after lining its nanopores with sizes similar to those of the RSAs. Such active layer constitution was found crucial for rejecting organic contaminants and achieving high water flux. These findings encourage further exploration of NF membrane preparation by molecular deposition as an attractive approach for constructing ultrathin membrane active layers to remove challenging contaminants with high water permeability.

Introduction

Nanofiltration (NF) membranes are capable of removing colloidal, organic, and ionic contaminants from water. As a result, NF membrane technology is emerging as an efficient and economical means of drinking water treatment.[1−3] Most commercial NF membranes have a composite thin-film configuration with a 50 μm thick layer (usually polysulfone) with asymmetric porous structure supporting a 100−200 nm thick active layer that is prepared by interfacial polymerization. The polymer active layer provides a barrier to water contaminants and determines membrane rejection capability and selectivity.

State-of-the-art commercial NF membranes have been developed to provide relatively high water permeability and high solute rejections when operated at low pressures by means of producing ultrathin polymeric active layers. Key achievements that have resulted in current state-of-the-art technology include (i) the breakthrough approach of Loeb and Sourirajan for preparation of anisotropic phase inversion (solution precipitation) membranes[4] and (ii) interfacial polymerization developed by Cadotte at North Star Research.[5] While the interfacial polymerization approach was a dramatic improvement with respect to both solute rejection and water permeability compared to the Loeb−Sourirajan process, additional progress on technique development to further decrease the thickness of the active skin has been slow. Moreover, in the last 20 years the chemical composition of the active layers of most commercial NF membranes has been limited to polyamide materials,[6] although some additional polymeric materials such as sulfonated polyethersulfone (SPES), polyvinyl alcohol (PVA) derivatives, and sulfonated polyphenylene oxide (SPPO) have also been developed.[7−10] Despite the satisfactory performance of the above membranes to remove salts and ionic contaminants, a general limitation is that they provide low selectivity and

* To whom correspondence should be addressed. Phone: (217) 244-4024; fax: (217) 244-8024; e-mail: moore@scs.uiuc.edu.

[†] Departments of Chemistry and Materials Science and Engineering, University of Illinois.

[‡] Department of Civil and Environmental Engineering, University of Illinois.

[§] Center of Advanced Materials for the Purification of Water with Systems, University of Illinois.

(1) American Water Works Association (AWWA) Membrane Technology Research Committee, *J. Am. Water Works Assoc.* **2005**, *97:8*, 79.

(2) Logsdon, G. S.; Horsley, M. B.; Freeman, S. D. N.; Neemann, J. J.; Budd, G. C. *J. Am. Water Works Assoc.* **2006**, *98:3*, 79.

(3) Baker, R. W. *Membrane Technology and Applications*; John Wiley & Sons Ltd.: England, 2004.

(4) Loeb, S.; Sourirajan, S. *Saline Water Conversion-II*; Advances in Chemistry Series 28; American Chemical Society: Washington, DC, 1963; pp 117−132.

(5) Cadotte, J. E. In *Materials Science of Synthetic Membranes*; Lloyd, D. R., Ed.; ACS Symposium Series 269; American Chemical Society: Washington, DC, 1985; pp 273−294.

(6) Chai, G.-Y.; Krantz, W. B. *J. Membr. Sci.* **1994**, *93*, 175−192.

(7) Ghosh, A. K.; Ramachandhran, V.; Hanra, M. S.; Misra, B. M. *J. Macromol. Sci: Pure Appl. Chem.* **2002**, *A39*, 199−216.

(8) Lang, K.; Sourirajan, S.; Matsuura, T.; Chowdhury, G. *Desalination* **1996**, *104*, 185−196.

(9) Immelman, E.; Sanderson, R. D.; Jacobs, E. P.; Van Reenen, A. *J. Appl. Polym. Sci.* **1993**, *50*, 1013−1034.

(10) Huang, Y. M.; Kim, J. J. *J. Appl. Polym. Sci.* **1984**, *29*, 4029−4035.

10.1021/cm070200a CCC: $37.00
Published on Web 05/31/2007

Table 1. Characteristics of Commercial NF Membranes[a]

	TFC-S	ESNA
manufacturer	Koch Membrane Systems, Inc.	Hydranautics Co.
active layer composition	polyamide	polyamide
nominal water flow	34.1 m^3/day	31.0 m^3/day
nominal solute rejection		
chloride	85%	
hardness	98.5%	
$CaCl_2$		89%

[a] Performance specifications provided by manufacturers for commercial spiral-wound elements with 37 m^2 (400 ft^2) of membrane surface area operated at 25 °C and 15% permeate recovery. Additional operating conditions: feed solution composition of 700 mg/L total dissolved solids with 45% of monovalent ions (TFC-S) or 500 mg/L $CaCl_2$ (ESNA), feed pressure of 0.55 MPa (TFC-S) or 0.52 MPa (ESNA), and pH 6.5−7.0 (TFC-S) or 7.5 (ESNA).

poor separation of small neutral molecules including micropollutants such as arsenic(III) (a human carcinogen present in many natural waters). To overcome this limitation, recent research efforts have focused on combining NF membrane technology with coagulation, preoxidation, or other processes.[11,12] Such hybrid treatment approaches, however, are less attractive because they lack the simplicity of using a single treatment step. Consequently, development of new NF membranes with active layers capable of providing a barrier against a broader range of water contaminants including small neutral molecules is desirable. Furthermore, because the water permeability per unit pressure increases inversely with the thickness of the membrane active layer, new methods are also needed to produce membranes with thinner active layers.

Because of the difficulty in controlling the thickness and limitations in varying the polymer chemistry of NF membrane active layers produced by phase-inversion polymer precipitation or interfacial polymerization, a new approach is needed. In our study, we are developing an approach to construct robust NF membrane active layers by first depositing rigid star amphiphiles (RSAs) on a modified polyethersulfone (PES) support membrane and then stabilizing the resulting film by chemical stitching of these building blocks. The RSAs are shape-persistent molecules[13] possessing a hydrophobic core which could anchor to the support membrane through noncovalent supramolecular interactions and multiple arms of side chains of various length and degree of hydrophilicity. A rigid star shape was thought to be crucial given earlier reports that linear molecules tend to snake through the microporous support membrane with significantly less retention than globular-shaped ones of the same molecular weight.[14]

In this paper, we describe the synthesis and characterization of RSAs with various levels of hydrophobicity and preparation of a first generation of NF membranes (RSAMs) with unstitched RSAs. After briefly summarizing the transport properties of these RSAMs including water flux and rejection of arsenic(III) and a surrogate organic contaminant Rhodamine WT (full details reported elsewhere),[15] results from membrane characterization by attenuated total reflectance Fourier transform infrared (ATR-FTIR) spectroscopy, field emission scanning electron microscopy (FE-SEM), atomic force microscopy (AFM), X-ray photoelectron spectroscopy (XPS), confocal microscopy, Rutherford backscattering spectrometry (RBS), and gas adsorption/desorption are presented. The most promising RSAMs are selected for active layer stabilization by chemical stitching in a subsequent phase of the study.

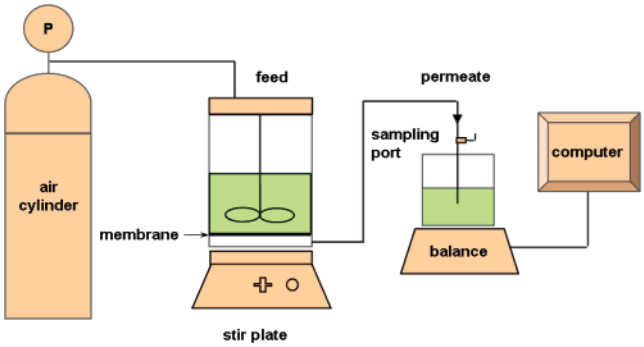

Figure 1. Diagram of experimental apparatus for fabrication and testing of RSAMs.

Experimental Section

Materials. The support layer used to deposit the active layers was a polyethersulfone (PES) ultrafiltration (UF) membrane model HFK-328 (Koch Membrane Systems Inc., Wilmington, MA). The PES dense skin film of this UF membrane was supported on a nonwoven polyester fabric bottom layer. The nominal molecular weight cutoff (MWCO) range specified for this UF membrane was 900−2300 Daltons. The UF membrane, received as a bulk roll, was machine cut into disk-shaped coupons with an effective membrane surface area of 41.8 cm^2 before use.

Two commercial NF membranes, TFC-S (Koch Membrane Systems Inc., Wilmington, MA) and ESNA (Hydranautics Co., San Diego, CA), were tested in this study for the purposes of providing a comparison to the performance of RSAMs. Relevant characteristics of the commercial membranes are listed in Table 1.

Experimental Setup. All RSAMs were prepared and tested using a bench-scale dead-end membrane filtration system (M8400, Millipore Co., Bedford, MA) (Figure 1). The transmembrane pressure was set at 0.34 MPa. Magnetic stirring was used for uniform deposition of the RSA materials onto the support membrane during RSAM preparation and minimizing solute concentration polarization during subsequent testing. WINWEDGE software (TAL Technologies Inc., Philadelphia, PA) was used for real-time data collection of permeate flux, which was measured gravimetrically with an analytical balance connected to a computer with a signal recording frequency of 5 s.

Test Contaminants. Rhodamine WT (R-WT, MW = 487, received as 35% (w/v) solution, Turner Designs, Sunnyvale, CA) and As(III) (H_3AsO_3, received as $NaAsO_2$ (99%), Sigma-Aldrich) were selected as solutes to test membrane performance. R-WT, a water-soluble dye approved for testing in drinking water treatment

(11) Floch, J.; Hideg, M. *Desalination* **2004**, *162*, 75−83.
(12) Sato, Y.; Kang, M.; Kamei, T.; Magara, Y. *Water Res.* **2002**, *36*, 3371−3377.
(13) For a recent review, see: (a) Zhang, W.; Moore, J. S. *Angew. Chem., Int. Ed.* **2006**, *45*, 4416−4439. For more reports, see: (b) Höger, S. *Chem. Eur. J.* **2004**, *10*, 1320−1329. (c) Wegner, G. *Macromol. Symp.* **2003**, *201*, 1−9.
(14) Baker, R. W. *J. Appl. Polym. Sci.* **1970**, *14*, 1197−1214.
(15) Suzuki, T.; Lu, Y.; Zhang, W.; Moore, J. S.; Mariñas, B. J. *Environ. Sci. Technol.*, submitted for publication.

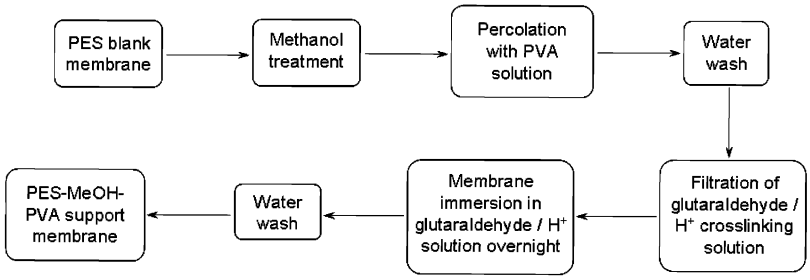

Figure 2. Schematic diagram for preparation of PES-MeOH-PVA support membrane.

Table 2. Water Permeability of PES, PES-MeOH, and PES-MeOH-PVA Supports[a]

membrane	water permeability (m/(day MPa))
PES	8.0 ± 0.5 ($n = 9$)
PES-MeOH	9.9 ± 0.8 ($n = 9$)
PES-MeOH-PVA	8.5 ± 0.6 ($n = 9$)

[a] The range of uncertainty is based on standard deviation results of n trials.

plants,[16] was chosen as a surrogate for organic contaminants. As(III), a drinking water contaminant regulated by the U.S. Environmental Protection Agency (EPA),[17] was selected as a representative neutral weak electrolyte poorly rejected by commercial NF membranes.

Membrane Performance Analysis. The performance of both commercial membranes and RSAMs was evaluated by measuring their water permeability and rejection of R-WT and As(III) at a constant pressure of 0.34 MPa, pH 6.0 ± 0.4, and 23 ± 2 °C. A solution containing 5 mg/L of R-WT and 4 mg/L of As(III) was used as feedwater for all membrane tests. The water permeability was monitored gravimetrically as described above. Solute rejection was calculated with the expression $SR = (1 - c_p/c_f) \times 100\%$ where c_f and c_p are the solute concentrations in the feed and product water, respectively. R-WT and As(III) concentrations were measured using fluorescence and UV spectroscopic methods, respectively.[15] The flux and rejection performance data were analyzed by parameter-fitting method using MATLAB software.[18]

PES-MeOH-PVA Support Membrane Preparation. The first step in RSAM fabrication was the in situ modification of the UF support membrane following the procedures depicted in Figure 2.[19] The PES membrane was installed in the cell of the membrane filtration system (Figure 1) and preconditioned by filtering distilled water through it for 10 min, followed by filtering methanol (50 mL) through it until the flux reached a plateau. The water permeability of the PES-MeOH membrane was found to be approximately 25% higher than that of unconditioned PES membrane (Table 2). Then, an aqueous PVA solution at a concentration of 1 mg/L was prepared by dissolving the polymer (Sigma-Aldrich, 99%+ hydrolyzed, 85 000−124 000 Daltons) in a sealed glass bottle with distilled water and magnetically stirred at 80 °C for 12 h. The PVA solution was filtered through the preconditioned PES membrane (PES-MeOH membrane). Both of these steps were carried out at room temperature and an operating pressure of 0.34 MPa. Filtration was stopped once a 15% reduction in permeate flux was reached relative to that of the PES-MeOH membrane. The excess PVA adsorbate on the membrane surface was removed by flushing with 100 mL of deionized water. Next, the PVA material adsorbed on the membrane was cross-linked by filtering a solution of 0.03 wt % glutaraldehyde and 0.00025 wt % acetic acid for 30 s and subsequently immersing the membrane in a solution of 0.03 wt % glutaraldehyde and 0.000025 wt % acetic acid overnight. Finally, the membrane was rinsed by filtering methanol (50 mL). Testing of the resulting PES-MeOH-PVA support membrane with pure water was found to have a stable permeate flux, approximately 10% lower than that of the PES-MeOH membrane (Table 2).

RSA Preparation. As shown in Scheme 1, three types of six-arm RSAs having various hydrophobic cores and hydrophilic side chains were synthesized and used to make membrane active layers. A measure of hydrophobicity for the various RSAs is provided in Table 3. RSA1−6 with polyphenylene hydrophobic dense cores were synthesized by a one-step cyclotrimerization[20] approach (Scheme 1(1 and 2)). RSA7 with a planar phenylene−ethynylene macrocyclic open core was synthesized by a recently developed one-step, cyclooligomerization via alkyne metathesis[21] (Scheme 1(3)). RSA8, a highly fluorescent dye emitting a yellow-green color, was obtained as a partial oxidative dehydrocoupling[22] product from RSA4 (Scheme 1(4)). A hexaiodo RSA derivative, RSA9, was synthesized by direct oxidative iodination of RSA4 (Scheme 1(5)). See Supporting Information for detailed preparation and characterization of RSAs.

Membrane Active Layer Formation. The active layers were prepared by filtering methanol solutions containing approximately 6 mg/L of each RSA through PES-MeOH-PVA supports at 0.34 MPa and 23 ± 2 °C using the apparatus in Figure 1. RSAMs with varied water permeability and contaminant rejection capability were prepared by manually controlling the decrease of water flux. The structure and performance of RSAMs with relatively high (5.3 ± 0.3 ($n = 6$) m/(day MPa)), medium (2.2 ± 0.1 ($n = 9$) m/(day MPa)), and low (1.6 ± 0.2 ($n = 9$) m/(day MPa)) water permeability were characterized (n is the number of replicate membranes tested to obtain these water flux values). More detailed performance characterization of these membranes is reported elsewhere.[15]

Membrane Characterization. RSAMs with medium water permeability and the corresponding PES, PES-MeOH, and PES-MeOH-PVA supports were characterized by FE-SEM, AFM, XPS, and ATR-FTIR spectroscopy. The pore size distribution of the PES-MeOH support was determined by gas adsorption/desorption. The RSAM fabricated with fluorescent RSA8 was also analyzed by confocal microscopy. RSAMs with high, medium, and low water permeability prepared with iodinated RSA9 were also characterized by RBS.

(1) FE-SEM. Commercial and modified membranes were observed with a field emission analytical scanning electron microscope

(16) http://www.turnerdesigns.com/t2/doc/appnotes/tracer_dye.html; Cortuvo, J. A., RHODAMINE WT AND B, *Memo to J. Warnquist*, dated Aug 2, **1988**.
(17) http://www.epa.gov/safewater/arsenic.html.
(18) http://www.mathworks.com/products/matlab/.
(19) PES-MeOH-PVA support membrane fabrication followed method described in Lang, K.; Sourirajan, S.; Matsuura, T.; Chowdhury, G. *Desalination* **1996**, *104*, 185−196 with some modification.
(20) Kobayashi, K.; Shirasaka, T.; Sato, A.; Horn, E.; Furukawa, N. *Angew. Chem., Int. Ed.* **1999**, *38*, 3483−3486.
(21) Zhang, W.; Moore, J. S. *J. Am. Chem. Soc.* **2004**, *126*, 12796.
(22) Hill, J. P.; Jin, W.; Kosaka, A.; Fukushima, T.; Ichihara, H.; Shimomura, T.; Ito, K.; Hashizume, T.; Ishii, N.; Aida, T. *Science* **2004**, *304*, 1481−1483.

Scheme 1. Synthesis of RSAs Used for RSAM Fabrication[a]

(1) RSA1-5 (6-arm star oligomers):

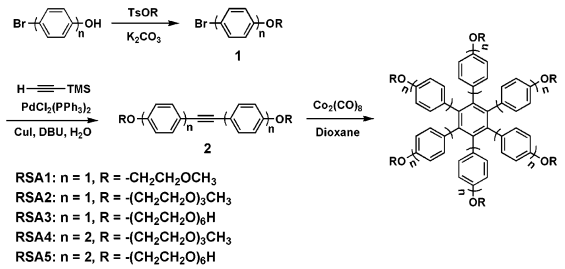

RSA1: n = 1, R = -$CH_2CH_2OCH_3$
RSA2: n = 1, R = -$(CH_2CH_2O)_3CH_3$
RSA3: n = 1, R = -$(CH_2CH_2O)_6H$
RSA4: n = 2, R = -$(CH_2CH_2O)_3CH_3$
RSA5: n = 2, R = -$(CH_2CH_2O)_6H$

(2) RSA6 (6-arm star oligomer):

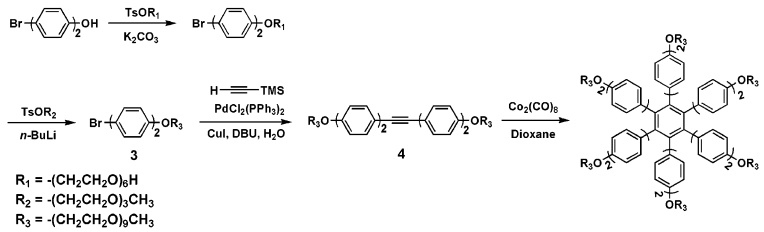

R_1 = -$(CH_2CH_2O)_6H$
R_2 = -$(CH_2CH_2O)_3CH_3$
R_3 = -$(CH_2CH_2O)_9CH_3$

(3) RSA7 (macrocycles):

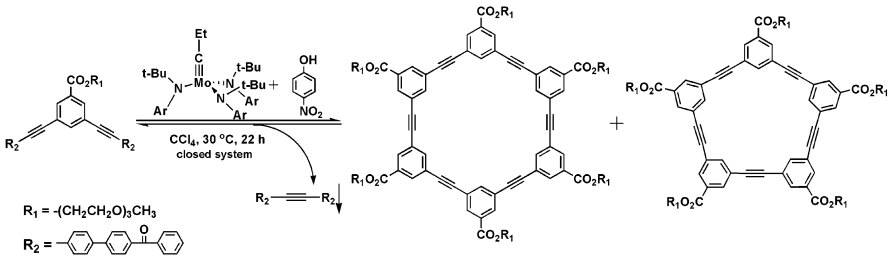

R_1 = -$(CH_2CH_2O)_3CH_3$

(4) RSA8 (6-arm star oligomer):

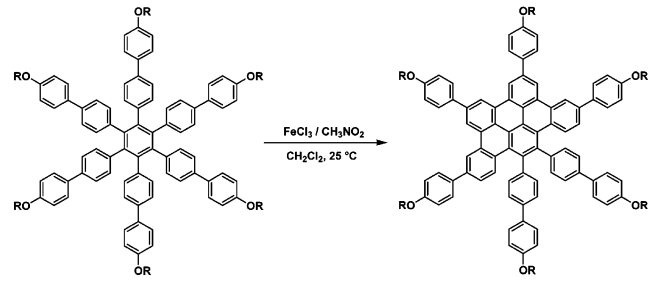

R = -$(CH_2CH_2O)_3CH_3$

(5) RSA9 (6-arm star oligomer):

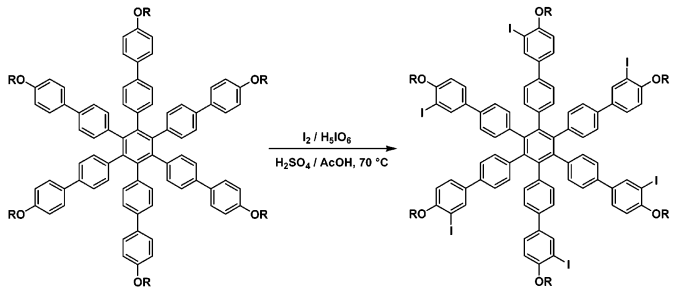

R = -$(CH_2CH_2O)_3CH_3$

[a] (1) Synthesis of dense-core RSA1−5 through cyclotrimerization. The products were purified by column chromatography. (2) Synthesis of RSA6 through cyclotrimerization. (3) Synthesis of open-core RSA7 through cyclooligomerization by alkyne metathesis. The product ratio of hexacycle to pentacycle is approximately 9 to 1 based on ^{1}H NMR integration. The mixture product was directly used without separating these two macrocycles. (4) Synthesis of fluorescent RSA8 through oxidative dehydrocoupling of RSA4. (5) Synthesis of RSAS9 through oxidative iodination of RSA4. See Supporting Information for molecular synthesis and characterization.

Table 3. Characteristics of RSAs

RSAs	diameter of hydrophobic core (nm)[a]	hydrophobicity ratio (area ratio)[b]	hydrophobicity (C/O)[c]
RSA1	1.1	0.307	5.0
RSA2	1.1	0.100	3.5
RSA3	1.1	0.042	2.7
RSA4	2.0	0.227	5.0
RSA5	2.0	0.102	2.9
RSA6	2.0	0.053	3.2
RSA7	1.7	0.155	3.8
RSA8	2.0	0.227	5.0
RSA9	2.0	0.227	5.0

[a] The diameter of hydrophobic core calculated using Cache software (version 6.1). [b] Hydrophobicity calculated as the area ratio of hydrophobic core to the hydrophilic side chains. [c] Hydrophobicity calculated as the element number ratio of carbon to oxygen.

(model JSM-7000F, JEOL), operated at a resolution of 1.5 nm (magnification of 10^5). The membranes were dried at 25 °C and coated with an Au/Pd layer at a thickness of approximately 4 nm prior to analysis.

(2) XPS. A Physical Electronics Kratos Axis XPS system was used to provide information about the surface composition of the prepared RSAMs. A monochromatic Al Kα (1486.6) X-ray source at a power of 105 W (voltage, 15 KV) was used, and the operating pressure was 10^{-9} Torr. High-resolution spectra of C 1s, S 2p regions (10−50 scans, 40 eV pass energy) were taken for each sample. XPS data were quantified by dividing the photoelectron peak areas by a relative atomic sensitivity factor and then taking each corrected peak area as a percentage of the total corrected peak area.

(3) AFM. Membranes were examined using an atomic force microscope (model Dimension 3100, Digital Instruments/Veeco). The instrument was operated in a tapping mode using silicon tips with nanometer scale resolution in air. The tip used for surface roughness analysis had a radius of 10 nm (BS-Tap300, Al coating, Nanoscience Instruments). For detection of ultrafine features, a 2 nm tip was used. Wet samples were dried at room temperature overnight and further irradiated with IR light for 20 min prior to testing.

(4) ATR-FTIR Spectroscopy. ATR-FTIR analyses were performed with a Nexus 670 FTIR apparatus (Thermo Electron Corporation, Germany) using a ZnSe crystal and OMNIC software for data processing. The membrane samples were predried overnight at 25 °C and then mounted face-to-face onto the crystal. Unpolarized IR light was irradiated onto the membrane surface with a nominal incidence angle of 45°.

(5) Confocal Microscopy. The confocal microscopy data was obtained using a Leica SP2 system (Leica Microsystems, Wetzlar, Germany) for 2D images. The samples were face-to-face mounted onto microscope slides with cover slips in wet condition (glycerol). The samples were excited with visible laser at $\lambda_0 = 351$ nm and imaged in fluorescence (384 nm $< \lambda <$ 544 nm) mode. The 2D images were processed with Leica Confocal Software (version 2.5, LCS Lite).

(6) RBS. Helium beams for Rutherford backscattering spectrometry (RBS) were generated by a 2-MeV Van de Graaff accelerator. The helium beam frequency applied was less than $10^{14}/cm^2$ (achieved by moving the sample continuously) to ensure the membranes were not damaged as confirmed from ATR-FTIR spectra. The RBS detector resolution was measured by testing a standard sample (5 Å thick gold film atop a layer of silicon). RBS data analyses were done with SIMNRA software.[23]

(23) http://www.rzg.mpg.de/~mam/.

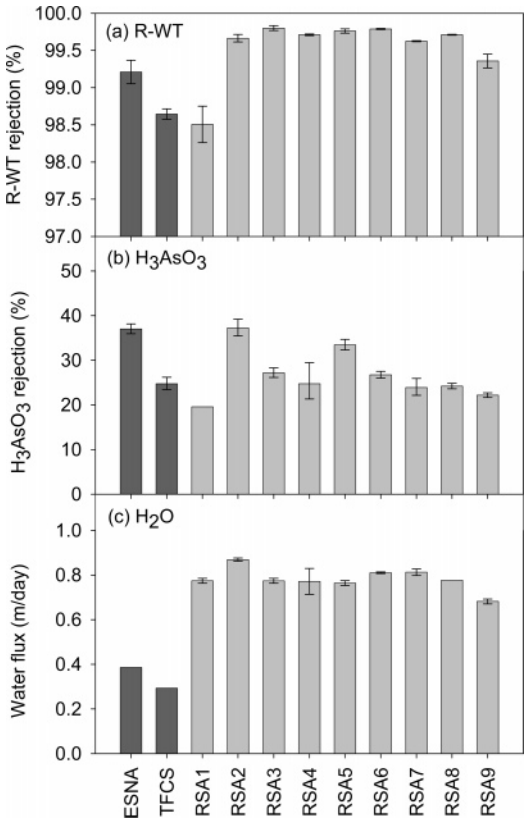

Figure 3. Comparison of water permeability and rejection capability of RSAMs (medium water permeability) with commercial TFC-S, ESNA membranes. Operating conditions: 0.34 MPa, 23 ± 2 °C, pH 6.0 ± 0.4. Water flux (m/day) = experimental permeability A (m/day·MPa) × pressure difference across the membrane Δp (MPa). Rejection data calculated based on equation solute rejection (%) = $\Delta p/(\Delta p + B/A)$ with $\Delta p = 0.34$ MPa; B represents contaminant permeation coefficient (m/day).[25] B values were obtained from parameter fitting of experimental data using MATLAB software. Standard deviation of RSAM water flux and rejection calculated based on two different hydrodynamic conditions (high mix and low mix).[15]

(7) Gas Adsorption/Desorption. The pore size distribution of the PES-MeOH support was determined by nitrogen gas adsorption/desorption using a Micromeritics Analyzer model ASAP2010. Membrane samples were predried in the desiccator for 2 days followed by oven drying at approximately 115 °C for 1 week. The pore size distribution was obtained by fitting the nitrogen desorption data with Barrett−Joyner−Halenda (BJH) model.[24]

Results and Discussion

Figure 3 shows a representative comparison of membrane performance and transport properties for commercial membranes and RSAMs prepared with medium water permeability, all tested at the same transmembrane pressure, pH, and temperature.[15] Performance data revealed that RSAMs had approximately 2−3 fold (0.7−0.9 m/day) higher water flux than that of the commercial TFC-S or ESNA membrane (0.3−0.4 m/day). With the exception of the membrane prepared with RSA1, rejection of R-WT was also significantly higher for all other RSAMs compared to those by commercial TFC-S and ESNA membranes (98.5−99.8% vs 98.6−99.2%). On the other hand, As(III) rejection varied for the different membrane materials. All RSAMs except the

(24) Barrett, E. P.; Joyner, L. G.; Halenda, P. P. *J. Am. Chem. Soc.* **1951**, *73*, 373−380.

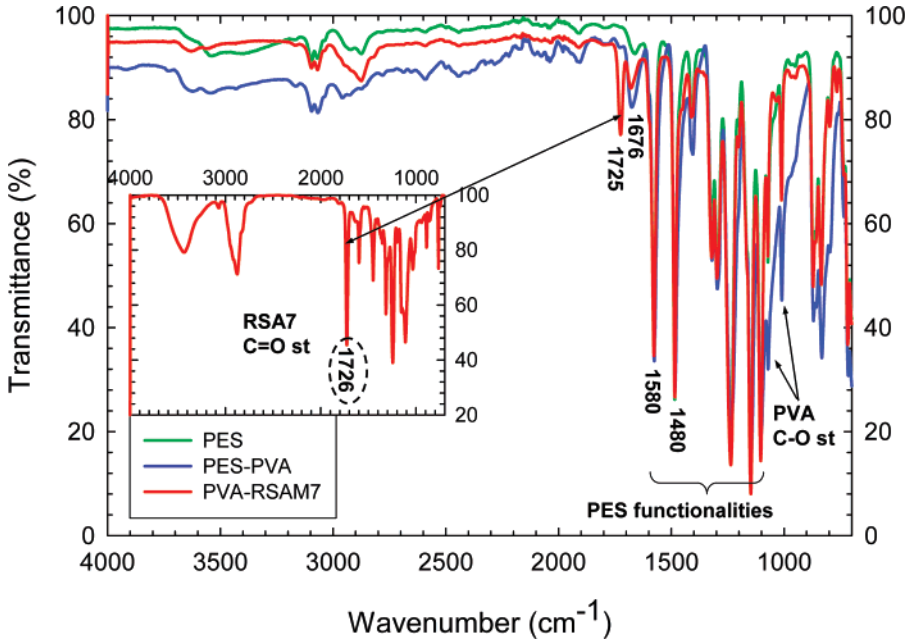

Figure 4. ATR-FTIR spectra of RSAM7, PES-MeOH-PVA support, and PES blank. (Inset) IR (KBr) spectrum of RSA7. The peak at the wavenumber of 1725 cm^{-1} of RSA7 confirmed the presence of RSA7 on the support membrane.

membrane prepared with RSA1 achieved similar or higher rejection compared to that for the commercial TFC-S membrane (22−37% vs 25%). In contrast, only the RSAM fabricated with RSA2 was capable of matching the As(III) rejection performance of the ESNA membrane (37%). Further performance analysis revealed a correlation between the hydrophobicity of RSAs and As(III) rejection (the most hydrophobic membrane RSAM1 showed the lowest rejection of As(III)).[15] This finding may provide a lead observation to guide future modifications of RSA materials or the synthesis of new structural units toward development of membranes with enhanced removal of As(III).

These promising membrane characteristics prompted us to perform physical and chemical characterizations of the above RSAMs with medium water permeability in order to elucidate the functional role of the RSAs. ATR-FTIR spectroscopy provided direct evidence of the presence of RSA7 within a depth of several micrometers[26] from the membrane surface. Although the ATR-FTIR spectra of RSAMs showed similar patterns of absorption bands dominated by the PES-MeOH-PVA support, the spectrum for RSAM7 showed a distinct band corresponding to the carbonyl stretching frequency of the ester functionality unique to RSA7 (characteristic band at 1725 cm^{-1}, Figure 4).

FE-SEM and AFM techniques were used to characterize the membrane's external surface morphology and roughness. FE-SEM images of RSAMs, PES-MeOH, and commercial TFC-S and ESNA membranes are shown in Figure 5. Due to the similarity of membrane surface morphologies of RSAMs, only RSAM3 and RSAM7 membranes are shown as representatives of dense-core and open-core RSA-modified membranes. As shown in Figure 5A,B, both TFC-S and

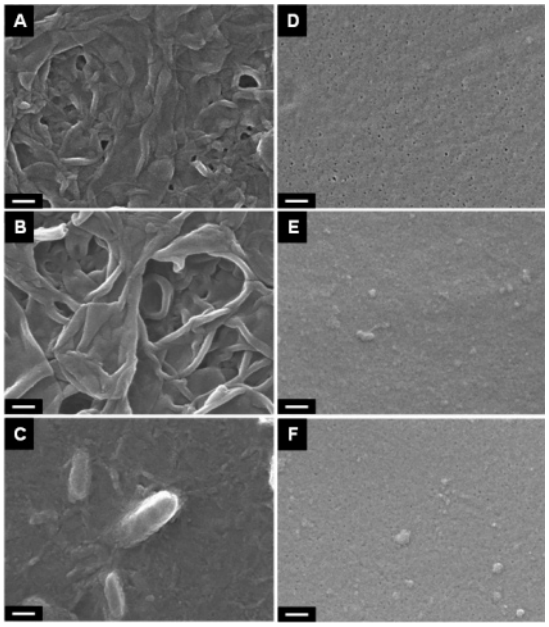

Figure 5. Representative FE-SEM images of membrane surfaces: (A) commercial TFC-S membrane; (B) commercial ESNA membrane; (C) commercial NTR-7450 membrane; (D) PES-MeOH membrane; (E) RSAM7 membrane; (F) RSAM3 membrane. Bars: 100 nm.

ESNA NF membranes which possess polyamide active layers have rough surface morphologies with the ESNA membrane being comparatively more structured than the TFC-S membrane. Another type of NF membrane, NTR-7450 (Nitto Denko Co., Japan), with an active layer composed of sulfonated PES (SPES) has protruding structures distributed over the entire surface as revealed by low-magnification observation. In contrast, PES-MeOH membrane support (Figure 5D), RSAM7 (Figure 5E), and RSAM3 (Figure 5F) are smooth, featureless, and largely unstructured.

Nanopores with an average diameter of approximately 10 nm (the Au/Pd coating might have resulted in slight shrinkage of the pore size) were observed on the surface of PES-MeOH

(25) Urama, R. I.; Mariñas, B. J. *J. Membr. Sci.* **1997**, *123*, 267−280.
(26) The detailed penetration depth depends on the refractive index difference between the ZnSe prism and the membrane samples.

support. These pores, through which nanosized water contaminants could pass by advection permeation,[25] are distributed at a density from approximately 5×10^2 to 8×10^2 pores/μm^2.[27] Interestingly, it was also found that the pores on the blank PES membrane without any treatment were only observed after filtering water (50 mL) under pressure (0.34 MPa). A statistically significant increase in pores was observed for the PES-MeOH membranes compared to the blank PES samples (Figure 5D). Following PVA treatment and deposition of RSAs, the number of pores per unit area significantly decreased and the size of pores shrank. The observed particles on top of the membrane surface (e.g., Figure 5E,F) are very likely due to accumulation of PVA, RSA, or a combination of both. Since the transmembrane water permeation through membrane nanopores is approximately proportional to the pore radius to the fourth power,[28] it could be safely assumed that the PVA/RSA treatment resulted in practical elimination of the advective flow through the nanopores. Because the water permeability decreased only from 9.9 m/(day MPa) for the PES-MeOH support to 8.0 m/(day MPa) for the RSAMs with highest water permeability, it could be concluded that the advective water transport through these largest pores of the PES-MeOH membrane was under 23% of its total water permeability. Although FE-SEM analyses provided useful information on membrane surface characteristics, they did not allow elucidating if the RSAs were located inside the support membrane pores, deposited atop the support, or distributed according to certain combination of these two configurations.[29]

Results obtained from AFM characterization of the surface topographies of RSAMs and commercial membranes were generally consistent with the FE-SEM observations. Preliminary AFM experiments were carried out in both air and liquid. However, it was found that the tapping mode AFM was unable to track the membrane surface with acceptable resolution.[30] Therefore, all subsequent AFM tests were performed in air using dry membranes. Although the observed root-mean-square (rms) roughness varied depending on local areas and scan ranges, the roughness generally increased in the order RSAMs < TFC-S < ESNA < NTR-7450 membranes in all scan ranges (Table 4).[31] The 3D AFM images at both magnifications (Figure 6) revealed that RSAM surfaces were flat and uniform compared to the three commercial membranes. The flatness of the skin layer may be a factor alleviating fouling problems associated with rough membrane surfaces leading to water flux decline during the filtration process due to the tendency to "valley clogging".[32] Although fouling phenomena are affected by many physicochemical factors, the relatively flat surface configuration of RSAMs developed in this study is an attractive characteristic.

Table 4. Comparison of RMS Roughness in 1 × 1 μm^2 and 5 × 5 μm^2 Scans[a]

membrane	1 × 1 μm^2 rms (nm)	5 × 5 μm^2 rms (nm)
TFC-S	17.9 ± 1.3 (n = 6)	21.4 ± 3.8 (n = 6)
ESNA	32.4 ± 11.9 (n = 6)	48.9 ± 3.7 (n = 6)
NTR-7450	32.9 ± 20.3 (n = 6)	66.7 ± 14.8 (n = 6)
RSAM7	1.7 ± 0.2 (n = 14)	4.7 ± 0.7 (n = 11)

[a] The range of uncertainty is based on standard deviation results of n trials.

Table 5. RMS Roughness Change in the RSAM Fabrication (1 × 1 μm^2 Scan)[a]

membrane	rms (nm)
blank PES	0.98 ± 0.27 (n = 9)
PES-MeOH	1.34 ± 0.14 (n = 12)
PES-MeOH-PVA	1.46 ± 0.14 (n = 16)
RSAM1	2.16 ± 0.25 (n = 10)
RSAM2	1.85 ± 0.17 (n = 6)
RSAM3	1.64 ± 0.19 (n = 9)
RSAM4	1.55 ± 0.15 (n = 12)
RSAM5	1.77 ± 0.17 (n = 6)
RSAM6	1.77 ± 0.18 (n = 18)
RSAM7	1.66 ± 0.17 (n = 14)
RSAM8	1.60 ± 0.07 (n = 8)
RSAM9	2.18 ± 0.27 (n = 24)

[a] The range of uncertainty is based on standard deviation results of n trials.

AFM analyses also provided information on the change in roughness as a result of the various membrane fabrication process steps. In general, roughness increased with each step: blank PES → PES-MeOH → PES-MeOH-PVA → RSAM (Table 5). These results were consistent with qualitative FE-SEM observations. Pores opened upon MeOH treatment, hence resulting in the slightly increased roughness in the first membrane fabrication step. Addition of PVA and RSA continued to increase the roughness only slightly, consistent with a greater mass of PVA/RSA accumulating first inside and then above the pores. Additional AFM evidence was obtained from 400 × 400 nm^2 scans of PES-MeOH and RSAMs using an ultrasharp tip with a radius of 2 nm. A comparison of 3D top-view and height images of RSAM7 and PES-MeOH support in Figure 7 revealed that even though there was a significant decrease in pore numbers after RSA modification, more pronounced peaks were observed on the surface of the RSAM consistent with its somewhat higher roughness. As depicted in panel A, the PES-MeOH membrane surface showed a network of ca. 10−15 nm wide dark regions with an average density from 6×10^2 to 8×10^2 pores/μm^2. Both the sizes and density of these features were close to those observed in the FE-SEM images. As shown in panel B, PVA/RSA addition resulted in loss of most of the dark regions, leaving the surface with slight protrusions and an increased surface roughness. These data suggest that most of the pores were plugged or covered by treatment with PVA/RSA.

(27) The density of pores is based on SEM results of 10 trials using different membrane pieces.
(28) Estimation based on Hagen−Poiseuille equation: $V = \pi R^2 \Delta p / 8 \eta l$ (R, pore radius; Δp, transmembrane pressure; η, viscosity; l, length of pores through the membrane).
(29) X-ray diffraction (XRD) was not successful due to the apparent random alignment of pores themselves and the detection limit of XRD for an ordered ultrathin polymer layer.
(30) This observation might be attributed to interference from the movable hydrophilic side chains of RSA adsorbates on the membrane surface.
(31) The 5 × 5 μm^2 scans and larger area scans are more precise than 1 × 1 μm^2 areas due to the large features on the membrane surface. The 1 μm^2 scans were found to be most appropriate for RSAMs to avoid scratches, dents, and contaminants introduced during the membrane fabrication process.

(32) Vrijenhoek, E. M.; Hong, S.; Elimelech, M. *J. Membr. Sci.* **2001**, *188*, 115−128.

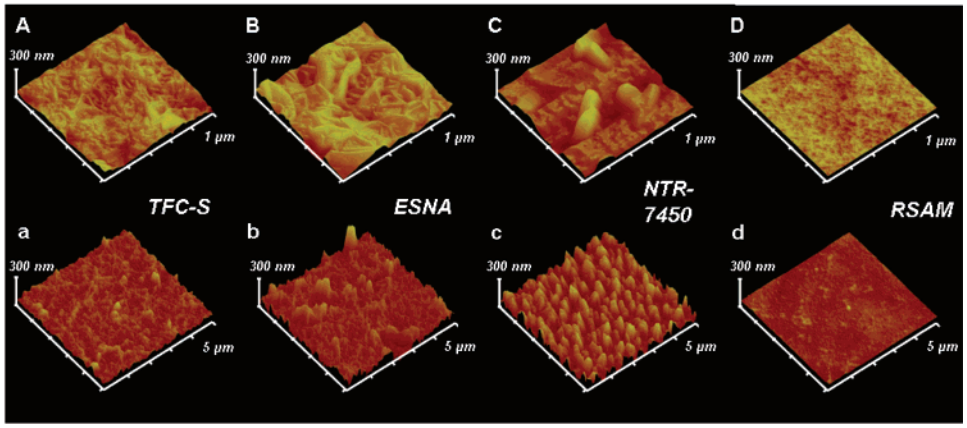

Figure 6. Representative AFM topography comparison of membrane surface roughness: (A, a) commercial TFC-S membrane; (B, b) commercial ESNA membrane; (C, c) commercial NTR-7450 membrane; (D, d) RSAM7 membrane. Upper scan: 1 μm × 1 μm. Lower scan: 5 μm × 5 μm. Height scale: 300 nm.

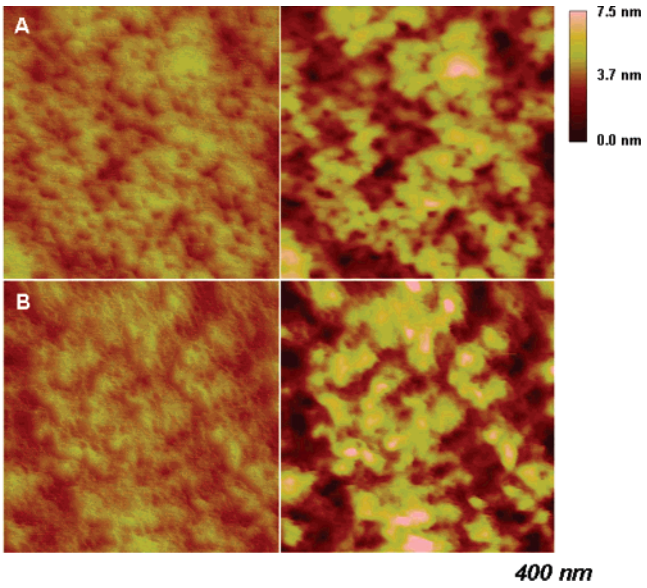

Figure 7. Representative AFM images of membrane surface topography over a 400 × 400 nm^2 region scale: (A) 3D (left) and top-view height (right) images of PES-MeOH support (scan rate, 1.196 Hz); (B) 3D (left) and top-view height (right) images of RSAM7 membrane (scan rate, 1.174 Hz). 3D image parameters: 0° rotation, 86° pitch, 131° light horizontal angle, 73° light vertical angle. Height image parameters: 0° rotation, top illumination (7.5 nm scale).

On the basis of the results obtained for the previously discussed ATR-FTIR spectroscopy, FE-SEM, and AFM analyses, two possible models (Figure 8) could be proposed for the configuration of the RSA active layer of the RSAMs: (i) RSA located mainly in a pure thin layer atop the PES-MeOH-PVA support (Model 1) and (ii) RSA located mainly within the pores of the PES-MeOH-PVA support (Model 2). To investigate the presence of a uniform, thin RSA layer on the PES support membrane, X-ray photoelectron spectroscopy (XPS) of all RSAMs and confocal microscopy studies of the fluorescent RSAM8 were also attempted. XPS data revealed no significant composition difference between the blank PES and RSAM1−8 membranes.[33] In contrast, confocal microscopy detected the presence of fluorescent RSA8 near the surface of the RSAM8. Membrane depth scans (*xyz* scan along the *z* axis) and cross-section scans (*xzy* scan along the *y* axis) revealed that RSA8 was located within a layer approximately 2 μm thick near the

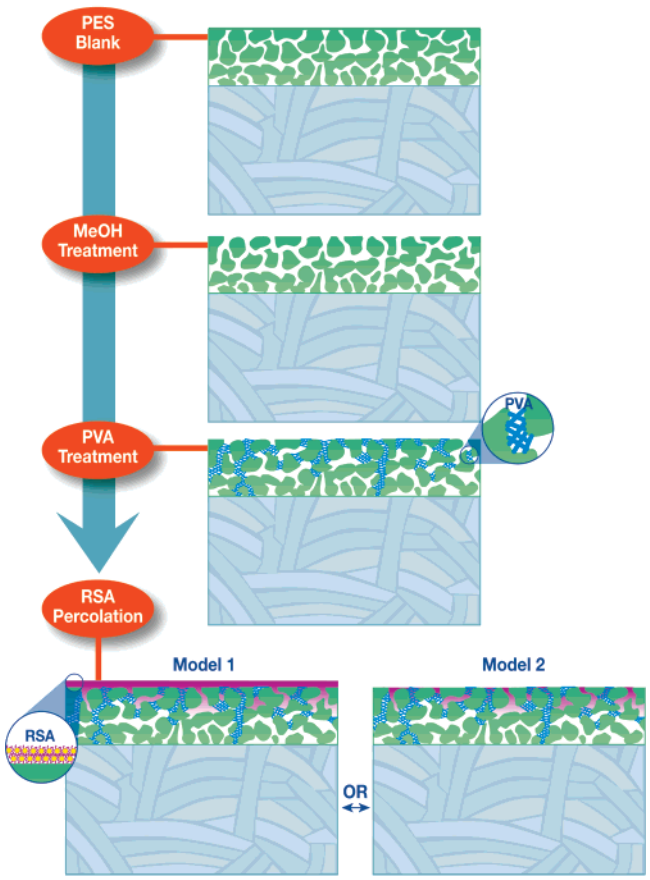

Figure 8. Flow chart of RSAM fabrication process, including three major procedures: MeOH treatment, in situ PVA plugging, and RSA percolation. Two models of RSAM active layer were proposed.

membrane surface (Figure 9). This finding was consistent with the previous ATR-FTIR results that showed RSAs are contained within a depth of several micrometers from the membrane surface. Unfortunately, the confocal images were unable to provide more precise information about formation of a pure fluorescent layer atop the support membrane (Model 1 in Figure 8) or whether the fluorescent

(33) High-resolution XPS study on the S 2p content (relative to the C 1s content) of the membrane external surface (<10 nm) did not provide evidence for a thin-layer surface model with significantly reduced or no S 2p signal. In this case, if a thin layer exists, the XPS signals are beyond the detection limit due to the loose packing of the RSAs.

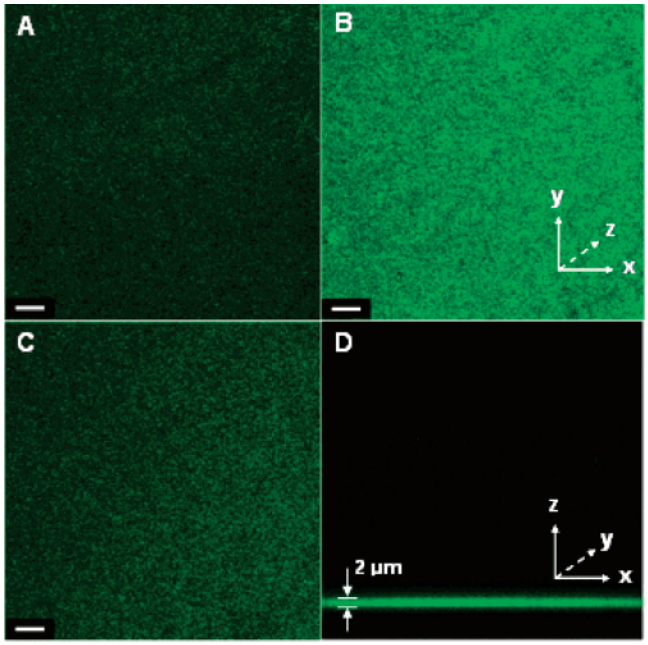

Figure 9. Representative confocal fluorescence images of RSAM8: (A) *xyz* view (perpendicular to the membrane surface) of fluorescent layer, 1 μm above the location reaching the maximum fluorescence focal plane among layer-by-layer scans along *z* axis (scan step size, 488 nm); (B) *xyz* view (perpendicular to the membrane surface) with maximum fluorescence among layer-by-layer scans along *z* axis (scan step size, 488 nm); (C) *xyz* view (perpendicular to the membrane surface), 1 μm away below the location of maximum fluorescence focal plane among layer-by-layer scans along *z* axis (scan step size, 488 nm); (D) *xzy* view (cross-section) of fluorescent layer along *y* axis (scan step size, 488 nm). Bars: 4 μm. Samples were prepared in wet condition (glycerol) and flattened by coverslips.

dye was distributed inside the support membrane pores (Model 2 in Figure 8).

Although some of the characterization techniques discussed above provided evidence of RSAs being present on or within the PES-MeOH-PVA support, it was still not possible to clearly identify or rule out the possible formation of an ultrathin pure RSA layer. In order to further investigate whether a thin layer exists, we carried out RBS experiments to provide a nondestructive depth profile of the elemental concentration and distribution in the membrane active layers following the method described by Mi et al.[34] for characterization of commercial NF membranes. By directing a helium-ion beam onto the membrane surface, helium particles can penetrate into the active layer as deep as approximately 2 μm and the resulting spectra of backscattering particles provides information on elemental composition as a function of sample depth. However, RBS spectra obtained for RSAM1−8 (data not shown) were not different from those obtained for the PES-MeOH-PVA support. This lack of discrepancy revealed that either these RSAs were located within the pores of the support or the film was too thin to be detected. Because the RBS signal increases with increasing atomic number and the signal for a heavier element would not be affected by those from the other elements present in the support membrane (C, O, S), the iodinated RSA9 was developed.

(34) Mi, B.; Coronell, O.; Mariñas, B.; Watanabe, F.; Cahill, D. G.; Petrov, I. *J. Membr. Sci.* **2006**, *282*, 71.

The RBS spectra obtained for RSAM9 membranes with high, medium and low water permeability are shown in Figure 10. Each RBS spectrum was characterized by a plateau signal for carbon stacked on top of a plateau signal for oxygen which in turn was stacked on top of a plateau signal for sulfur. This part of the spectra was undistinguishable from the overall spectra for RSAM1−8 and PES-MeOH-PVA support (not shown). In contrast, the RBS spectra for the RSAM9 also included distinct iodine signals. The overall intensity of the iodine signals increased with increasing mass of RSA9 applied; a membrane with higher water flux had lower RSA9 mass applied and so a less pronounced iodine signal. Besides the variation in overall signal intensity, the RBS band shape for the membrane with high water permeability lacked the frontal peak at the energy onset of the signal (ca. 1810 KeV) observed for membranes with medium and low water flux. A broad peak at lower energy was observed for all three membranes.

The elemental concentration as a function of sample depth was determined by fitting the three spectra with SIMNRA.[34] The best fit was obtained by assuming that RSA9 was present both inside pores for all three RSAMs and forming a film atop the support for the medium and low water flux membranes. In addition, the dip observed between the frontal narrow and broader peaks for the medium and low water permeability membranes (Figure 10) supported that RSA9 was present at a lower concentration inside the support membrane area immediately adjacent to its external surface compared to the RSA9 concentrations deeper in the support and in the external film. The lower concentration of RSA9 would be consistent with the pores near the surface of the support being smaller than the molecular size of RSA9 (molecular diameter ca. 4.4 nm). The pore size distribution of a PES-MeOH membrane sample obtained by nitrogen gas adsorption/desorption measurement revealed that approximately 0.1% of its total pore volume corresponded to pores with diameters below approximately 4 nm. Considering the asymmetric nature of the PES membrane, it would be reasonable to assume that the smallest pores would be located near its surface, thus resulting in the observed RSA9 depleted layer. Finally, the broader iodine peak signals of the spectra revealed that maximum RSA9 adsorption was achieved at a certain depth and that the concentration decreased with increasing depth. This observation would be consistent with the asymmetric nature of the support in which the adsorption capacity would be more pronounced in pores of similar size to that of the adsorbate and would decrease with increasing pore size.

On the basis of the preceding discussion the following simplifying assumptions were made to fit the experimental iodine spectra with SIMNRA: (1) a layer of pure RSA9 was present atop the support (Model 1 in Figure 8) for the RSAMs with medium and low permeability, (2) RSA9 was absent in a thin layer next to the support interface, and (3) RSA9 was distributed in a series of subsequent sublayers at constant concentration within each sublayer (Model 2 in Figure 8). The third assumption of stepwise decrease in RSA9 concentration was made because a gradual change in iodine concentration could not be fitted with SIMNRA.

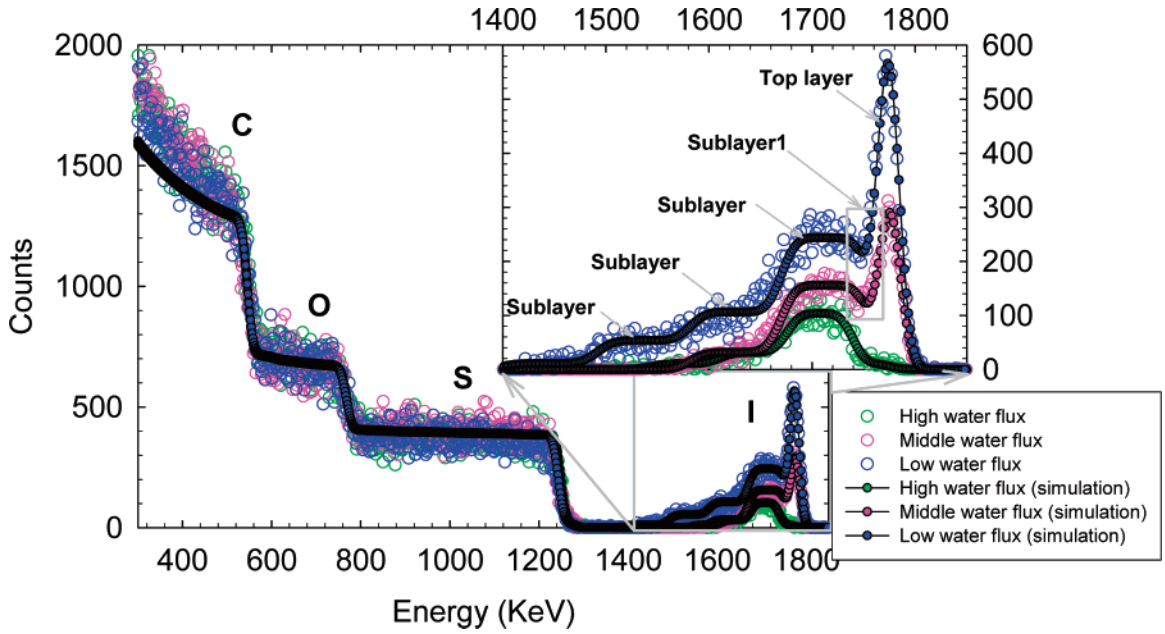

Figure 10. RBS comparison analysis of membranes prepared from RSA9 with different categories of water fluxes (high, medium, low).[15]

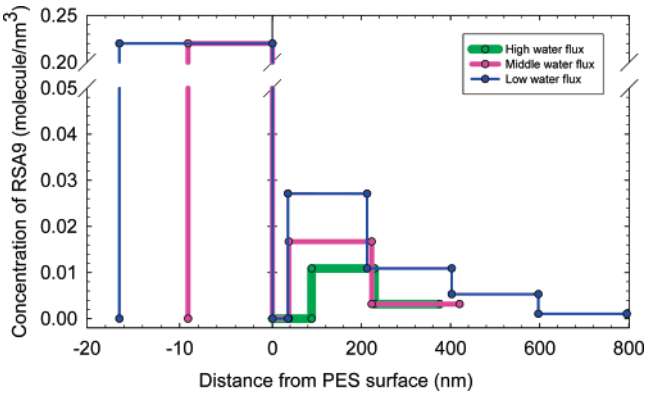

Figure 11. Concentration distribution of RSA9 across the membrane thickness based on the RBS analysis of RSAM9 membranes with high, medium, and low water permeability. Note: positive distance toward the inside of the membrane support.

As depicted in Figure 10, the SIMNRA simulations provided a good representation of all three RBS spectra. The corresponding simulated molecular distribution of RSA9 across the membrane thickness is summarized in Figure 11. A comparison of the three RBS spectra supported that the deposition process was characterized by RSA9 first only accumulating inside the PES (Model 2, Figure 8) and subsequently continuing the internal adsorption with simultaneous build up of a thin layer of pure RSA9 atop the surface (a hybrid of Models 1 and 2 in Figure 8). Permeation data presented elsewhere[15] revealed that measurable rejection of R-WT and As(III) above the performance of the PES-MeOH-PVA support required the presence of the thin layer of RSA9 on top of the support and thus that the active layer was responsible for the NF characteristics.

The RBS-simulated concentration profile also provided estimates for the thickness of the active layer and the various sublayers inside the support. By assuming various thicknesses of the RSA active layer the simulated spectra were best fit to the sharp front peak observed in the experimental spectra.[35] The best fit revealed that the active layers of the medium and low water flux membranes were 9.1 ± 4.1 and 16.5 ± 6.3 nm, assuming that the density of the pure RSA9 layer was 1 g/cm^3. It is interesting to notice that both of these active layers were significantly thinner than the active layer of the commercial ESNA (100 nm) and TFC-S (85 nm) NF membranes.[34] According to the RBS simulations, RSA9 was absent in a layer next to the interface with a thickness of approximately 40 nm and adsorbed in subsequent layers each with a thickness of about 185 nm. This thickness was based on the assumption that the porosity of all sublayers was the same as the average porosity of ~20% obtained for the PES-MeOH sample from the gas adsorption/desorption analyses. Notice that the overall simulated penetration depth of RSA9, approximately 1 μm, was in good agreement with the confocal microscopy observation that RSA9 was located within a 2 μm thick layer near the substrate surface. Finally, although active layer thickness is only one of several factors affecting water permeability across organic thin films, the two- to three-fold higher water permeability observed for the medium flux RSAMs compared to that of the commercial NF membranes (Figure 3) was consistent with the difference in active layer thickness. However, it was also likely that RSA9 adsorbed in the various sublayers of the support provided additional resistance to water permeability, and thus, the enhancement in water permeability is not as pronounced as it could have been if RSA9 would have only been present in the active layer.

(35) The active layer thicknesses quantified in this study, however, have uncertainties introduced by systematic errors in spectra fitting with SIMNRA and other experimental errors (approximately ± 15% for each; experimental errors include determination of detector resolution, incident angle, and fwhm (full width at half maximum) of incident energy). The membrane roughness was not taken into consideration during simulation as results from AFM study revealed RSAMs have almost flat membrane surfaces with low RMS values. The validity of active layer thicknesses also depends on the density assumption during conversion of molecular concentration to thickness. The assumed density in this study was 1 g/cm^3 (approximately ± 15% error) across the entire membrane thickness.

Conclusions

A new generation of NF membranes was developed by direct percolation of six-arm, rigid star amphiphiles (RSAs) through methanol/PVA-conditioned PES (PES-MeOH-PVA) UF membranes. The observed NF performance of these RSA membranes (RSAMs) was associated with formation of an ultrathin active layer of pure RSA atop the PES-MeOH-PVA support. FE-SEM and AFM analyses both revealed that the resulting active layers possessed uniform flat surfaces with lower roughness compared to those of commercial TFC-S, ESNA, and NTR-7450 membranes. Additionally, confocal microscopy provided visual evidence regarding the location of RSAs within a 2 μm thick layer, whereas RBS simulation further elucidated a possible membrane-forming process which included sequential internal PES-MeOH-PVA support pore plug in and surface layer build up of pure RSA. The ultrathin active layers (9−16 nm) provided rejection for the organic contaminants surrogate Rhodamine WT (R-WT) and contributed to the As(III) rejection and water flux enhancement. Of special significance, RSAMs with ultrathin active layers achieved comparable or higher rejection capabilities of As(III) and R-WT compared to the commercial NF membranes while having two- to three-fold increase in water flux, which led us to envision further study of the RSAMs as an optimal model system. The next research phase will focus on polymerization or chemical stitching of RSAs with the goal of stabilizing the active layers as well as further exploration of functionalities and structural properties, such as hydrophobicity levels, that might be essential to achieve high rejection of As(III).

Acknowledgment. This work was supported by the National Science Foundation Science and Technology Center of Advanced Materials for the Purification of Water with Systems (WaterCAMPWS) (grant no. CTS-0120978). We thank the Center for Microanalysis of Materials at the University of Illinois at Urbana−Champaign, which is partially supported by and the U.S. Department of Energy (grant no. DEFG02-91-ER45439), for providing FE-SEM, AFM, XPS, and RBS instrumentation. We also thank Jim Mabon for his help with the SEM images and Doug Jeffers for his help with RBS experiments.

Supporting Information Available: Synthetic procedures and characterization for RSA1−9. This material is available free of charge via the Internet at http://pubs.acs.org.

CM070200A